

# Triassic closure of South Tianshan Ocean: Evidence from provenance analysis of High-Pressure relics-bearing fore-arc sediments and multi-disciplinary data

zhou tan

Xinjiang Institute of Ecology and Geography, Chinese Academy of Sciences <https://orcid.org/0000-0003-0235-0306>

Wenjiao Xiao (✉ [wj-xiao@mail.iggcas.ac.cn](mailto:wj-xiao@mail.iggcas.ac.cn))

Chinese Academy of Sciences, Urumqi, Xinjiang 830011, China <https://orcid.org/0000-0003-3518-0526>

Qigui Mao

Hao Wang

Miao Sang

Rui Li

Limin Gao

Yuhong Guo

Jingmin Gan

Yanhong Liu

Bo Wan

---

## Article

### Keywords:

**Posted Date:** April 26th, 2022

**DOI:** <https://doi.org/10.21203/rs.3.rs-1551759/v1>

**License:**  This work is licensed under a Creative Commons Attribution 4.0 International License.

[Read Full License](#)

---

**Version of Record:** A version of this preprint was published at Communications Earth & Environment on October 31st, 2022. See the published version at <https://doi.org/10.1038/s43247-022-00578-4>.

# Abstract

A major debate concerning the final welding time of southern Altaids has led to considerable uncertainty regarding the configuration of northeast Pangea and the reconstruction of proto-Asia. Here we report Triassic provenance deposited in a fore-arc accretionary basin closely located with the Akeyazi LT-UHP metamorphic complex in the South Tianshan Orogenic Belt (STOB). Field-based detrital zircon U-Pb analysis of sandstones yield a maximum depositional age of the early Triassic ( $\sim 231.7 \pm 1.1$  Ma) with a major early Permian peak and few Precambrian records. Hf isotopic analysis, accompanying with multi-disciplinary data compilation, indicate the early Triassic sediment received additional detritus from distal juvenile East Tianshan Arc region, rather than from any proximate tectonic units or a missed intra-oceanic arc. A hypothesis is proposed for STOB geodynamic model with introducing temporary flat subduction beneath the Central Tianshan Arc region. Available data advocates the STO, which serves as an accessory ocean basin paleo-geographically belonging to the Paleo-Asian Ocean, may have been closed in the early Triassic.

## Introduction

Asia, as the largest extant accretionary continent, was made by the successive amalgamation of numerous magmatic arcs, continental blocks and accretionary complexes from the Paleozoic to Cenozoic<sup>1,2</sup>. The Altaids (Fig. 1a), extending from the Pacific Ocean in the east to the Ural Mountains in the west, witnessed the shaping of Gondwana and Pangea from the late Neoproterozoic to early Mesozoic<sup>3-6</sup>. The final suturing of the southern Altaids was proposed to occur from the late Devonian, through the Carboniferous to the late Permian-mid Triassic<sup>6-12</sup>. Nevertheless, the exact docking time of the Karakum-Tarim cratons with the southern Altaids is highly of debate, which in turn gives rise to uncertainties on final closure of the Paleo Asian Ocean (PAO) and the timing of their integration into Pangea. The South Tianshan Orogenic Belt (STOB) in the southern Altaids (Fig. 1a) marks the suturing of the Kazakhstan-Yili-Central Tianshan Continent (KYCTC) with the Karakum-Tarim cratons as the South Tianshan Ocean (STO) closed. In the last decade, numerous studies from igneous and metamorphic petrology, sedimentology and geochronology have been conducted to investigate geodynamic evolution of the STOB. Yet little consensus has been made on the most speculative debate, i.e., the timing of the final collision, Triassic<sup>11,13</sup> versus late Carboniferous<sup>12,14-17</sup>. This is probably due to complicated structural and metamorphic overprinting during long-lasting accretionary histories.

Sedimentary basins that formed in intra-oceanic fore-arc environment, whereas basins overlying relatively mature crust would be less likely to deform due to their cold and stiff lithospheric roots, are more likely to survive collisional orogenesis, even if juxtaposed against weaker accretionary complexes<sup>18</sup>. Forearc basins may contain a sedimentary documentation of much longer duration than the time the arc front has been active, as in the Mariana arc<sup>19</sup>, and serve as sensitive recorders of tectonic processes accompanied with orogenic cycle. In this study, we focus on a newly discovered, undeformed fore-arc accretionary basin. It is closely located to the south with the Akeyazi LT-UHP metamorphic complex

(AMC), which bears plentiful findings of coesite<sup>20,21</sup> in various lithologies. Previous studies mainly focused on the recovery of P-T-time condition of high grade metamorphized lithologies<sup>22,23</sup> and their exhumation histories, however, scarce attentions had been paid on regional accretionary basins. Integration of field mapping, detrital zircon U-Pb and Lu-Hf and trace elements analyses have been conducted to provide evidence for the deposition time and provenance of studied sandstone in the Muzitekexie fore-arc accretionary basin (MFAB). Additional multi-disciplinary evidence was also compiled from regional various lithologies to fingerprint the temporal-spatial variations of detrital deposition and mantle “signal” characteristics. Available data allows to discuss the nature of the MFAB, final closure of the PAO (as witnessed by the western accessory ocean basin, the STO) and implications for subduction processes along with regional geodynamics.

## Results

**The Akeyazi metamorphic complex.** The Altaids is a long-lasting composite collage between the East European craton, Siberian craton, Karakum-Tarim Craton and the North China craton (Fig. 1a). The present 2500 km-long STOB (check the Supporting Information for the detail of regional geological setting), located in the southern Altaids, extends from the western deserts of Uzbekistan, Tajikistan, Kyrgyzstan and Kazakhstan to the northern Xinjiang in China and marks the final amalgamation between the Tarim and Siberian cratons<sup>1,5,7,13,24,25</sup>. The Chinese STOB are divided, from north to south, into the Kazakhstan-Yili-Central Tianshan Continent (KYCTC) and South Tianshan accretionary complex (AC<sup>14,26</sup>, including the South Tianshan Belt, STB), and bounded to the south, by the North Tarim Fault (NTF) with the North Tarim Craton (NTC). To East, the geographical South Tianshan is separated, by Toksun-Kumishi High Road<sup>27</sup> (along longitude ~89 °E), as the Central Tianshan (CTS) and East Tianshan (ETS). The AMC constitutes the eastern part of the Kazakhstan collage system within the Altaids and extends for about 200 km along the South Central Tianshan Fault (SCTF, Fig. 1b), and correlates with the Atbashi<sup>28-30</sup>, Chatkal<sup>31,32</sup> and FanKarategin (U)HP metamorphic complexes<sup>33</sup> in the Kyrgyzstan and Tajikistan parts of the STOB. Our study area is closely adjacent to the south with the AMC, as a ~1.5 km N-S across, fore-arc accretionary basin (located at the branch of Akeyazi river, named as Muzitekexie valley, Fig. 1b-d) resting unconformably on top of the greenschist-facies unit and clamped between the SCTF and the local greenschist-UHP detachment fault (GUHPD). To south, it is closely associated with the regional LT-UHP unit, which bearing plentiful findings of coesite<sup>20,21</sup> and predominantly composed of strongly schistosed meta-volcanoclastics hosting mafic metavolcanics as pods, lenses, boudins, thin layers or massive blocks<sup>34</sup> and marble horizons<sup>20</sup>. In contrast, studied MFAB is mainly constituted of undeformed sandstones with minor cobble conglomerate blocks and local carbonaceous mudstone seams. Obvious sedimentary bedding and climbing ripples (Fig. 1e) are well developed in sandstone. The conglomerate blocks wrapped within the sandstones have sizes ranging from tens of centimeters to several meters, and are matrix-supported and polymictic with poorly sorted, angular and clastic quartzites (Fig. 2b).

**Sampling strategy.** To acquire the age of the MFAB and provenance information of the sedimentary rocks, several sandstone and conglomerate samples were collected for petrographic, mineralogical and

geochemical studying. In addition, systematically sampling of sandstone samples, over different outcrops in the MFAB, were conducted for bulk-rock major and trace elements composition analysis (Table S1) and the in-situ LA-ICP-MS U-Pb chronological and Lu-Hf isotopic measurements of detrital zircon (Tables S2-4).

**Collective Aggregation of Regional Multiple Geochronological and Geochemical Data.** To thoroughly evaluate the geodynamic evolution of STOB-KYCTC-NTC subduction-collision system as witnessed by the formation of the MFAB, we fingerprint the spatial and temporal variations of regional detrital deposition and magma source characteristics, based on systematic geochemical and chronological data collection from various lithologies among the KYCTC, AC and ETS regions (data from NTC region is also provided for comparison, Figs. 5, 6, 7). This included: 1) 503 intermediate rocks with complete major and trace elements compositions, radiometric ages and bulk-rock Sr-Nd isotopic data (Table S6); 2) 2591 zircon Lu-Hf isotopic data, together with ages, from igneous and sedimentary rocks (Table S7); 3) 7350 detrital zircon U-Pb ages from sedimentary rocks (Table S8). We then utilized zircon  $\epsilon\text{Hf}(t)$ , together with bulk-rock Sr/Y,  $\epsilon\text{Nd}(t)$ , and Nb/Yb elemental ratios, and detrital zircon age spectrum as proxies to differentiate magmatism with distinct source signatures and sedimentary detritus provenance. Furthermore, a compilation (Table S9) of 140 age data of regional metamorphism, depositing and main strike-slip faulting and thrusting events was also conducted from chronological comparison.

**Petrography.** Studied sandstones are mainly composed of medium- to fine-grained (100-400  $\mu\text{m}$  across) sub-angular to moderate-abraded quartz, cemented by calcite (Fig. 2a, 2c), implying comparatively moderate to long distance transportation of detritus prior to deposition. Compositionally, sandstones of the MFAB are mainly composed of quartz and lithic grains but lack feldspar (Fig. 2g). The dominate lithic fragments are intermediate to acid volcanic rocks with microlithic and lathwork textures (Fig. 2a-c). In addition, high pressure mineral relics (i.e., omphacite, phengite and rutile), which has similar solid-solution composition to those from the adjacent southern HP-UHP metamorphic complex (Fig. 2h-i), were found either as inclusions in sub-angular quartz grains (Fig. 2d) or as fragments around them (Fig. 2f).

**Bulk-rock geochemical composition.** The results of bulk-rock major and trace elements composition and detrital zircon U-Pb age, rare earth elements and Lu-Hf isotopic composition of analyzed sandstone samples are respectively presented in Tables S1-4. Bulk-rock major elements data (Fig. 3a-b) suggest a composition ranged between litharenite and greywacke, with relatively lower CIA (chemical index of alteration)<sup>35</sup> and higher ICV (index of compositional variability)<sup>36</sup> values compared to those of PAAS (post-Archaean Australian shales<sup>37</sup>). Compositions of trace elements (Fig. 3c-f) of studied sandstone show obviously higher abundance of La and Th and lower concentration of Hf with respect to poorly sorted sediments from oceanic island arc but reflecting similarity with those from active continental margin.

**Detrital zircon U-Pb and Lu-Hf isotopes.** The age data of detrital zircons are plotted as KDEs and histograms (Figs. 4a-b, 6c) using *isoplotR*<sup>38</sup>. CL images of representative detrital zircon grains with age, U concentration and Th/U ratio are shown in Figure S1. In addition, diagrams of ages versus detrital zircon

rare earth elements characters (denoted by  $\delta\text{Eu}$ ,  $(\text{Lu}/\text{Tb})_N$  and REEs pattern, Fig. 4c-g) are also made to deduce the multiple detritus provenance. A total of 213 spots of detrital zircon U-Pb ages (Fig. 4a-b) were analyzed for sandstone samples in the MFAB. Most of zircon grains are subhedral to euhedral characterized with obvious oscillatory zoning (Fig. S1). They display comparable Precambrian and Paleozoic-late Triassic U-Pb age spectrum ( $\sim 227$ - $1765$  Ma) of detrital zircon on the KDE plot (Figs. 4b, 6c). About three-quarters and less than one-tenth of chronological analysis respectively yield late and early Paleozoic ages, far more than the amount ( $\sim 14\%$ ) of Precambrian age records. Thereinto, one major age peak is concentrated at  $\sim 290$ - $296$  Ma ( $\sim 74\%$ ), with minor Devonian-Precambrian ages at  $\sim 410$ ,  $\sim 711$ ,  $\sim 930$ ,  $\sim 1199$  and  $\sim 1765$  Ma. To be stressed, a certain amount ( $\sim 4\%$ ) of Triassic ages are reported with weighted average at  $231.7 \pm 1.1$  Ma (MSWD=6.3,  $n=4$ , Figs. 4b, 6c). The trace elements characters of analyzed detrital zircons are complicated, with various Th/U ratio (0.184-2.394) likely indicating assorted detritus provenance. Most of them (including four youngest Triassic zircon grains) show REEs pattern with obvious LREEs and HREEs slopes ( $(\text{Lu}/\text{Tb})_N > 4$ ) and strong negative Eu abnormal ( $\delta\text{Eu} \sim 0.4$ , Fig. 4c-d), suggesting a possible inherited Igneous origin<sup>39</sup>. In addition, a part of  $\sim 300$  Ma and  $\sim 315$  Ma detrital zircon grains, respectively, display strong negative Eu abnormal ( $\delta\text{Eu} \sim 0.3$ ) and gradual HREEs ( $(\text{Lu}/\text{Tb})_N \sim 3$ ) and inconspicuous negative Eu abnormal ( $\delta\text{Eu} \sim 1.0$ ) and HREEs plateau ( $(\text{Lu}/\text{Tb})_N \sim 1$ - $2$ , Fig. 4c-g), implying metamorphic derivations, which similar to regional zircons overgrew under greenschist- and blueschist/eclogite-facies conditions<sup>21</sup>. The Hf isotopic compositions of most of detrital zircon ( $\sim 67\%$ ) in sandstones yield contrasting  $\epsilon\text{Hf}(t)$  values from  $-18.4$  to  $+18.2$  (Fig. 7a). Thereinto, Triassic-Permian detrital zircons have broadly positive  $\epsilon\text{Hf}(t)$  values from  $-1$  to  $+10$ .

## Discussion

**Deposition Timing and Provenance Analyses.** Since sedimentary rocks cannot be deposited before their constituent particles are formed, the youngest detrital zircon grains in a given deposit constrain the maximum depositional age<sup>40</sup>. This “the law of detrital zircons<sup>41</sup>” is widely proved to be effective in sedimentary basins among numerous tectonic settings<sup>42,43</sup>. The MDA is consistent with the true depositional age (TDA) of sediments if their depositional sites are proximal to magmatic arcs<sup>43</sup>. Our study shows that sandstones from different outcrops in the MFAB exclusively yield Paleozoic-late Triassic ages with only a few Precambrian records. Thereinto, among the prominent early Permian ( $\sim 290$ - $296$  Ma) age peak, a significant early Triassic population ( $\sim 5\%$ , Figs. 4a-b, 6c) is identified ( $231.7 \pm 1.1$  Ma, MSWD = 6.3,  $n = 4$ ). This implies that the timing of deposition of studied sedimentary strata extended, at least, to the early Triassic.

To conduct the provenance analysis, 2591 zircon Lu-Hf isotopic data, together with ages, from igneous and sedimentary rocks and 7350 detrital zircon U-Pb ages from sedimentary rocks are compiled for comparison. The detrital zircon age spectrums of regional sedimentary rocks sampled on the assumed upper plate (KYCTC), the accretionary wedge (AC, including the STB) and the passive lower continental plate (NTC) are presented in Fig. 6. Sediments from both of above tectonic units (Fig. 5a) display

significant amounts (~ 36–77%) of Precambrian detritus population, in contrast with those (< 15%) from Yili Basin and the MFAB in this study. For early Mesozoic-Paleozoic detrital records: 1) sediments from the STB and NTC show consistently binary age peaks, respectively, at 270–310 and 400–500 Ma, interpreted as the reflection of Tarim Permian mantle plume<sup>44–46</sup> and temporarily active continental arc developed in the North Tarim Margin during the Silurian-Ordovician<sup>44,46–49</sup>; 2) broadly continuous early Mesozoic-Paleozoic detrital records characterize the age spectrum of sediments from the AC, KYCTC and Yili Basin, serving as the response of continuous arc magmatism during the north-ward subduction of Paleo STO<sup>14,50</sup>. Overall, none of any similarity of detrital zircon age spectrum can be identified, from above tectonic units (Fig. 5a), with respect to that of the MFAB (Fig. 6). Besides, Triassic inherited zircon ages are very rare in region, with only one report<sup>11</sup> but with eclogite-facies metamorphic origin. This further implies that a local deposition for the detritus provenance of studied sandstones in the MFAB is probably not of possibility, unless a missed Triassic intra-oceanic arc was in fact existed, but have not been found yet. However, the relatively high ICV values (Fig. 3b) of studied sandstone, which imply an immature source typical of active continental margin setting<sup>36</sup>, and the Th-La-Hf concentrations fairly deviated from detritus provenance from oceanic island arc<sup>51</sup> (Fig. 3c-d) essentially rules out this possibility. To be stressed, the identification of minor high-pressure mineral relics-bearing detritus (Fig. 2c-f) and corresponding ~ 315 Ma detrital zircons with Bs/Ec-facies metamorphic origin (Fig. 4c-g) in studied sandstones indicate that at least a few of detrital materials (but not the majority) are deposited from an additional proximal provenance.

A distal source is then of necessity to be considered. The western part of ETS, which extends to the most eastern side of geographic Chinese South Tianshan until the Xingxingxia Fault (Fig. 1a), is also clamped between the KYCTC and the NTC<sup>26</sup>. Considerable quantity of Triassic igneous rocks had been reported in the ETS region, especially those with adakitic geochemical affinity<sup>52,53</sup>. According to our data compilation for intermediate rocks among the Central Tianshan-Yamansu arc, two major age peaks, respectively at ~ 230–240 and ~ 280–290 Ma (Fig. 6e) characterize the ETS arc magmatism, and it is completely distinct from those in the KYCTC and the NTC. Such an age pattern, as well as relatively positive  $\epsilon\text{Hf}_{(t)}$  value, of the ETS arc intermediate rocks (Fig. 6e), in fact, broadly resembles that of detrital zircon from sandstones in the MFAB (Figs. 4a-b, 6c), implying a potential distal provenance from the ETS region. Additional evidence comes from the sub-angular to moderate-abraded shape (although not all, Fig. 2a, 2c) of most of detritus and these Triassic detrital zircon grains (Fig. S1) in sandstones, which suggests a relatively moderate to long distance of transport, for example via contour current<sup>54</sup>, prior to their deposition. This speculation is also supported by the presence of climbing ripples on sandstone outcrop (Fig. 1e) which advocate a depositing environment with high suspension load current<sup>55</sup>. Moreover, the long-lasting (late Carboniferous-early Triassic) regional nearly W-E trend strike-slip movements (as we compiled in Fig. 7f), mainly along the SCTF (Fig. 1a), could also facilitate the trench-paralleled transportation of detritus drive by contour current.

**The final closure of the South Tianshan Ocean.** It is of challenges to constrain the timing of final closure of a long-lived accretionary subduction system. Miscellaneous methods such as the timing of a regional

unconformity, bimodal magmatism, stitching plutons, and extensional deformation were used to constrain the time of final closure of the South Tianshan Ocean, which consequently led to different conclusions. Much of viewpoints, for the issue of the final closure of the STO among the STOB in the southern Altaids, had been proposed (as reviewed by ref<sup>14</sup>). Some authors argued the final assembly of southern Altaids occurred along the North Tianshan Suture Zone in the late Carboniferous subsequent to the collision of the KYCTC and NTC during late Devonian to early Carboniferous times<sup>7,10,56,57</sup>. This model is mainly based on the following assumptions that: 1) the regional angular unconformity during late Devonian-early Carboniferous times was related to the collision of the STB and the KYCTC, 2) eclogite-facies peak metamorphism as reflected by the UHP terranes took place at ~ 350 – 345 Ma, and 3) top-to-north thrusting of the UHP rocks over the KYCTC resulted from south-ward oceanic subduction. Alternatively, some authors<sup>14</sup> suggested the final suturing of southern Altaids was achieved by northward subduction of the South Tianshan Ocean and subsequent collision of the KYCTC and the Karakum-Tarim cratons at ~ 320 Ma, based on below arguments: 1) ~ 320–330 Ma ophiolite/ophiolitic mélange had been identified as the youngest MOR-type ophiolite along the SCTF (in Guluogou and Wuwamen areas<sup>14,58</sup>), broadly consistent with the timing of LT-UHP eclogite-facies metamorphism in Akeyazi and Atbashi areas<sup>21,22,31</sup>; 2) the latest Carboniferous molasse-type conglomerate overlying the Atbashi (U)HP rocks<sup>28</sup>, and the ~ 285 Ma post-orogenic S-type leucogranite dike crosscutting the Akeyazi UHP complex<sup>12</sup>; 3) the resumption of widespread magmatism in the STB and the NTC at ~ 270–310 Ma<sup>59–62</sup>.

It is worth noticed, yet, a significantly younger Permian (~ 265 Ma) MOR-type ophiolitic mélange<sup>63</sup> from the Bindaban area in the eastern Central Tianshan along the SCTF, the late Carboniferous radiolarian<sup>64</sup> in chert from Kyrgyzstan Atbashi range, and the late Permian radiolarian<sup>65</sup> in clastic rock from Chinese western South Tianshan had been recently identified, further jointly advocating the possible existence of a much younger ocean basin in the southern Altaids. This speculation is echoed by the find of ~ 300 Ma glaucophane-bearing BS/GS facies meta-volcanoclastic units in Akeyazi metamorphic complex which suggests the subduction of the Paleo STO was probably still active during late Carboniferous<sup>22</sup>. In addition, the concept that “the metamorphic age of deeply recovered high grade protolith formation constrains the timing of oceanic closure and/or continental collision” only works in place where late exhumation associated with oceanic closure and continental subduction occurred (Yet, only found in the western Alps, New Caledonia and Central Cuba)<sup>66</sup>. This further implies that most of metamorphic age of deeply recovered high grade rock essentially has no link with the timing of oceanic closure. Recent work<sup>22</sup> also highlighted that the final juxtaposition, at crustal level, of the diverse sub-units with various metamorphic grades making the metamorphic dome in the AMC could have occurred at around ~ 280–290 Ma, broadly consistent with the regional ~ 285 Ma crosscut post-orogenic S-type leucogranite dike<sup>12</sup>, prior to the STO closure. Moreover, the preservation of climbing ripples (Fig. 1e), petrographic characters of Triassic zircon population (and most of detritus, Figs. 2a, 2c, S2) and the detrital zircon age pattern of studied sandstones in the MFAB, jointly call for the existence of a relatively board ocean basin (Fig. 8), until the early Triassic, to facilitate relatively moderate to long distance of detritus transport, likely via

contour current<sup>67</sup> with high suspension load current<sup>55</sup>, from a potential distal provenance in the ETS region.

In short, our new data, integrated with the compilation of regional multi-disciplinary evidence, suggest that oceanic subduction could be still operating until the early Triassic in the STOB. Such Triassic closure of accessory ocean basins, which paleo-geographically belongs to the PAO, were reported among the Altaiids, e.g., the Kanguer accretionary mélange in East Tianshan<sup>68</sup>, the Alxa block<sup>42</sup>, central Inner Mongolia<sup>69</sup> and Solongker suture zone<sup>70,71</sup>, implying that the PAO closed almost synchronously along the western, central and eastern parts of the Altaiids.

**Trench-parallel slab geometry “anisotropy” and geodynamic implication.** Relatively fast and young oceanic plate that subducts beneath less steep plate, including horizontal slab segments, is known as the Peru-Chile type subduction<sup>72</sup>, with symbolic features like marginal subduction erosion, inboard migration of upper-plate deformation and weak to absent arc magmatism<sup>73</sup>. Its rareness<sup>74</sup> and remarkable influences on overlying continental plate<sup>73</sup> and economically important ore deposits<sup>75</sup> make it of great significance and diagnostic especially for ancient orogens<sup>76,77</sup>.

To reconcile numerous controversies, we suggest the possibility of flat subduction tectonics, providing an alternative hypothesis (Fig. 8) for the geodynamic model of the STOB. Common models, whatever advocating mainly north- or south-ward subduction beneath the KYCTC<sup>12,14</sup> or the NTC<sup>10,78</sup>, all based on a priori assumption that the down-going STO slab is ultimately coherent object with almost no topographical and geometrical “anisotropy” (i.e., differences). In fact, significant impacts on the CTS arc magmatism during the Carboniferous, by trench-perpendicular topographical “anisotropy” (i.e., seamount chain<sup>79</sup>), had been highlighted in region, calling for the possible existence of trench-parallel slab geometry “anisotropy” during the north-ward subduction of the paleo STO.

As we presented above, studied early Triassic, HP mineral relics-bearing sandstones likely received detritus mainly from distal provenance—the ETS region whose arc magmatism characterize by similar age (broadly, also the  $\epsilon_{\text{Hf}}(t)$ , Fig. 7a) pattern of Triassic population with a major early Permian peak (Figs. 4a-b, 6c). In this case, at least a part of geographical ETS region (i.e., the west side of Xingxingxia fault, Fig. 1a), which previously has not been considered yet, is non-negligible with respect to the geodynamic model of the STOB<sup>12,50,78</sup>. According to our compilation (Fig. 7), the age gap of ~ 220–280 Ma, between the continuous ETS (~ 220–330 Ma) and the intermittent CTS (~ 280–330 Ma, Fig. 5) arc magmatism, is speculated as the period of the absence of CTS arc magmatism, during which crustal thickening (Fig. 7b) and mantle “signal” soaring (Fig. 7a, 7c, 7d) in the ETS are accompanied. Such phenomenon is well observed in present-day Chilean subduction zone where area suffered from flat subduction is characterized by to-some-extent broadening (in trench-parallel and -perpendicular directions) of magmatic arc and subsequent cessation of magmatism<sup>74,80,81</sup>. In addition, Nd-Hf isotopic decoupling (Fig. 7g) is evident for Permian arc magmatic rocks in the CTS region, suggesting a “zircon effect” because of the addition of subducted terrigenous sediments into magma sources<sup>82</sup> and could imply the

Permian arc magmatic in the CTS region was derived from a mixed mantle source due to the interaction between arc inherited magmatism and upwelling magma of oceanic lithosphere induced by flat subduction and potential subsequent slab rollback, although such a decoupling was interpreted as the inducing of the activity of Tarim Plume<sup>17</sup>. Flat subduction could be also facilitated by strong discontinuities in the oceanic (i.e., oceanic plateau and seamount chain as the buoy<sup>83</sup>) and overriding plates structure (craton and micro-continent with fairly deep Moho depth<sup>67</sup>). Similar processes had, in fact, been identified in region, coincidentally supporting the speculation of temporary flat subduction beneath the CTS region during the north-ward subduction of paleo STO: 1) Long-lasting Carboniferous-Devonian seamount chain subduction<sup>79</sup>; the relative thickened crust, which could maintain extra compositional buoyancy, of seamount, oceanic plateau and aseismic ridge effectively prohibit the slab from sinking into the mantle<sup>84,85</sup>; 2) Localized micro-continent with cratonic lithosphere were identified among the CTS region<sup>86,87</sup>, and their spatial distribution (as revealed by Hf isotope contour map; Fig. 5c) is broadly in coincidence with the area where the early Triassic to early Permian absence of CTS arc magmatism is confirmed with speculated flat subduction; numerical modeling shows that a thick cratonic root can increase the magnitude of suction acting on the subducting plate due to the mantle wedge flow and this suction effect will vary along strike if craton has a finite width<sup>88,89</sup>. Other features associated with flat subduction, for example the crustal contractional deformation (e.g., in Mexican<sup>90</sup>) and migration of arc volcanism (e.g., in Chile, Andes<sup>72</sup>), had not been observed yet in the STOB, and are probably overprinted by the pervasive nearly W-E trend strike-slip deformation<sup>22,91,92</sup> along the SCTF (Figs. 1a, 6f).

## Methods

**Bulk-rock major and trace elements analysis.** Major elements compositions were analysed at the Institute of Geology and Geophysics, Chinese Academy of Sciences (IGGCAS). Major oxides were determined by a PHILLIPS PW1480 X-ray fluorescence spectrometer (XRF) on fused glass disks. Loss on ignition (LOI) was measured after heating to 1000°C. Uncertainties for most major oxides are ca. 2%, for MnO and P<sub>2</sub>O<sub>5</sub> ca. 5%, and totals are within 100 ± 1 wt.%. Whole rock Fe<sub>2</sub>O<sub>3</sub> content is constrained by potassium permanganate titration. Trace element concentrations were analyzed by inductively coupled plasma mass spectrometry (ICP-MS) using a Finnigan MAT ELEMENT spectrometer at the IGGCAS. Relative standard deviations (RSD) are within ± 10% for most trace elements but reach ± 20% for V, Cr, Co, Ni, Th and U according to analyses of rock standards. Detail major and trace elements analyses are presented in Table S1.

**LA-ICP-MS Zircon U-Pb Dating and trace elements composition.** Zircons were separated from samples processed by crushing, heavy-liquid, and magnetic methods and then were mounted in epoxy resin and polished to expose the interior. Cathodoluminescence (CL) imaging was conducted with a scanning electron microscope at the Institute of Geology and Geophysics, Chinese Academy of Sciences (IGGCAS), to select suitable grains and optimal target sites for the U-Pb dating and Lu-Hf isotopic analyses. U-Pb dating and trace elements composition of zircon were simultaneously conducted by LA-ICP-MS at the

Wuhan SampleSolution Analytical Technology Co., Ltd., China. Detailed operating conditions for the laser ablation system and the ICP-MS instrument and data reduction are the same as in ref<sup>93</sup>. Laser sampling was performed using a GeolasPro laser ablation system that consists of a COMPexPro 102 ArF excimer laser (wavelength of 193nm and maximum energy of 200 mJ) and a MicroLas optical system. An Agilent 7700e ICP-MS instrument was used to acquire ion-signal intensities. Helium was applied as a carrier gas. Argon was used as the make-up gas and mixed with the carrier gas via a T-connector before entering the ICP. A “wave” signal smoothing device is included in this laser ablation system<sup>94</sup>. The spot size and frequency of the laser were set to 60  $\mu\text{m}$  and 6 Hz, respectively, in this study. Zircon 91500 and glass NIST610 were used as external standards for U-Pb dating and trace element calibration, respectively. Each analysis incorporated a background acquisition of approximately 20–30 s followed by 50 s of data acquisition from the sample. An Excel-based software ICPMSDataCal was used to perform off-line selection and integration of background and analyzed signals, time-drift correction and quantitative calibration for trace element analysis and U-Pb dating<sup>95</sup>. Concordia diagrams and weighted mean calculations were made using Isoplot/Ex\_ver3<sup>96</sup>. Relevant data is listed in Tables S2 and S3.

**LA-ICP-MS Zircon Lu-Hf Isotopic Analysis.** In situ zircon Hf isotopic analyses were conducted on the same spots where U-Pb analyses were made. Hf isotopic compositions were determined by a Neptune MC-ICP-MS equipped with Geolas Plus 193 nm ArF excimer laser at the Wuhan SampleSolution Analytical Technology Co., Ltd., China. A laser spot size of 40  $\mu\text{m}$  and a laser repetition of 8 Hz with energy density of 15  $\text{J}/\text{cm}^2$  were used during the analyses. The signal collection model was one block with 200 cycles, with an integration time of 0.131 s for 1 cycle and a total time of 26 s during each analysis. Zircon 91500 was used as external standard for Hf isotopic analyses and was analyzed twice every 5 analyses. Replicate analyses of 91500 yielded a mean  $^{176}\text{Hf}/^{177}\text{Hf}$  ratio of  $0.282300 \pm 24$  ( $2\sigma$ ,  $n = 82$ ), which is concordant with the  $^{176}\text{Hf}/^{177}\text{Hf}$  ratios, measured by Goolaerts et al. (2004). The detailed analytical procedures are described in Wu et al. (2006). Relevant data is listed in Table S4.

**Microprobe Analysis.** In situ major element compositions of garnet and inclusion minerals were obtained from polished thin sections by electron microprobe analyses at the the Wuhan SampleSolution Analytical Technology Co., Ltd., China, with the use of JEOL JXA 8100. Quantitative analyses were performed using wavelength dispersive spectrometers with an acceleration voltage of 15 kV, a beam current of 15 nA, a 3  $\mu\text{m}$  beam size and 30 s counting time. Natural minerals and synthetic oxides were used as standards, and a program based on the ZAF procedure was used for data correction. Results of representative microprobe analyses of identified HP minerals in studied sandstone samples are presented in Table S5.

## Declarations

## Data Availability

The authors declare that all data supporting the findings of this study are available within the article and its Supplementary Information files.

# Acknowledgements

This study was financially supported by the National Natural Science Foundation of China (41888101, 42002241). A special acknowledgment is expressed to the project of the China-Pakistan Joint Research Centre on Earth Sciences (131551KYSB20200021) that supported the implementation of this study. This is a contribution to IGCP 662.

## Author contributions

Z. T. and W. X. conceived the study. Z. T. Z. T., Q. M., H. W., S. M., R. L., L. G., Y. G., J. G., B. W. conducted field geological exploration and sample collection. Z.T., Y. L. and B. W. conducted the experimental analyses and data collection. Z. T. conducted data processing and visualizing. Z. T., W. X., Q. M. and B. W. contributed to the interpretation of the results and wrote the manuscript.

## Competing interests

The authors declare no competing interests.

## Additional information

**Supporting information** is available for this paper at:

**Correspondence and requests** for materials should be addressed to Z. T. (tanzhou@ms.xjb.ac.cn) and W. X. (wj-xiao@mail.iggcas.ac.cn).

## References

1. Şengör, A. M. C., Natal'in, B. A. & Burtman, V. S. Evolution of the Altaid tectonic collage and Palaeozoic crustal growth in Eurasia. *Nature* **364**, 299–307 (1993).
2. Xiao, W. *et al.* Paleozoic multiple subduction-accretion processes of the southern Altai. *Am. J. Sci.* **309**, 221–270 (2009).
3. Cawood, P. A. *et al.* Accretionary orogens through Earth history. *Geol. Soc. Spec. Publ.* **318**, 1–36 (2009).
4. Han, Y. *et al.* Tarim and North China cratons linked to northern Gondwana through switching accretionary tectonics and collisional orogenesis. 95–98 (2016). doi:10.1130/G37399.1
5. Windley, B. F., Alexeiev, D., Xiao, W., Kröner, A. & Badarch, G. Tectonic models for accretion of the Central Asian Orogenic Belt. *J. Geol. Soc. London.* **164**, 31–47 (2007).

6. Xiao, W. *et al.* A Tale of Amalgamation of Three Permo-Triassic Collage Systems in Central Asia: Oroclines, Sutures, and Terminal Accretion. *Annu. Rev. Earth Planet. Sci.* **43**, 477–507 (2015).
7. Charvet, J. *et al.* Palaeozoic tectonic evolution of the Tianshan belt, NW China. *Sci. China Earth Sci.* **54**, 166–184 (2011).
8. Han, B. F., He, G. Q., Wang, X. C. & Guo, Z. J. Late Carboniferous collision between the Tarim and Kazakhstan-Yili terranes in the western segment of the South Tian Shan Orogen, Central Asia, and implications for the Northern Xinjiang, western China. *Earth-Science Rev.* **109**, 74–93 (2011).
9. Han, Y. *et al.* Detrital zircon provenance constraints on the initial uplift and denudation of the Chinese western Tianshan after the assembly of the southwestern Central Asian Orogenic Belt. *Sediment. Geol.* **339**, 1–12 (2016).
10. Wang, B. *et al.* Paleozoic tectonics of the southern Chinese Tianshan: Insights from structural, chronological and geochemical studies of the Heiyingshan ophiolitic mélangé (NW China). *Tectonophysics* **497**, 85–104 (2011).
11. Zhang, L. *et al.* Triassic collision of western Tianshan orogenic belt, China: Evidence from SHRIMP U-Pb dating of zircon from HP/UHP eclogitic rocks. *Lithos* **96**, 266–280 (2007).
12. Gao, J. *et al.* The collision between the Yili and Tarim blocks of the Southwestern Altaids: Geochemical and age constraints of a leucogranite dike crosscutting the HP-LT metamorphic belt in the Chinese Tianshan Orogen. *Tectonophysics* **499**, 118–131 (2011).
13. Xiao, W., Windley, B. F., Allen, M. B. & Han, C. Paleozoic multiple accretionary and collisional tectonics of the Chinese Tianshan orogenic collage. *Gondwana Res.* **23**, 1316–1341 (2013).
14. Wang, X. *et al.* Final Assembly of the Southwestern Central Asian Orogenic Belt as Constrained by the Evolution of the South Tianshan Orogen: Links With Gondwana and Pangea. *J. Geophys. Res. Solid Earth* **123**, 7361–7388 (2018).
15. Gao, J. *et al.* Tectonic evolution of the South Tianshan orogen and adjacent regions, NW China: Geochemical and age constraints of granitoid rocks. *Int. J. Earth Sci.* **98**, 1221–1238 (2009).
16. Klemd, R., Gao, J., Li, J. L. & Meyer, M. Metamorphic evolution of (ultra)-high-pressure subduction-related transient crust in the South Tianshan Orogen (Central Asian Orogenic Belt): Geodynamic implications. *Gondwana Res.* **28**, 1–25 (2015).
17. Han, Y. *et al.* Plume-modified collision orogeny: The Tarim-western Tianshan example in Central Asia. *Geology* **47**, 1001–1005 (2019).
18. Busby, C. & Pérez, A. A. Tectonics of sedimentary basins: Recent advances. (2011).
19. Taylor, B. & Fujioka, K. 42. RIFTING AND THE VOLCANIC-TECTONIC EVOLUTION OF THE IZU-BONIN-MARIANA ARC1. in *Proc. ODP. Sci. Results* **126**, 627–651 (1992).
20. Bayet, L., John, T., Agard, P., Gao, J. & Li, J. L. Massive sediment accretion at ~80 km depth along the subduction interface: Evidence from the southern Chinese Tianshan. *Geology* **46**, 495–498 (2018).
21. Tan, Z. *et al.* P–T–time-isotopic evolution of coesite-bearing eclogites: Implications for exhumation processes in SW Tianshan. *Lithos* **278–281**, 1–25 (2017).

22. Tan, Z. *et al.* Architecture and P-T-deformation-time evolution of the Chinese SW-Tianshan HP/UHP complex: Implications for subduction dynamics. *Earth-Science Rev.* **197**, 102894 (2019).
23. Xiao, W. *et al.* Accretionary processes and metallogensis of the Central Asian Orogenic Belt: Advances and perspectives. *Sci. China Earth Sci.* **63**, 329–361 (2020).
24. Alexeiev, D. V *et al.* Tectono Stratigraphic Framework and Palaeozoic Evolution of the Chinese South Tianshan 1. *Geotectonics* **2**, 3–35 (2015).
25. Dolgoplova, A. *et al.* Geodynamic evolution of the western Tien Shan, Uzbekistan: Insights from U-Pb SHRIMP geochronology and Sr-Nd-Pb-Hf isotope mapping of granitoids. *Gondwana Res.* **47**, 76–109 (2017).
26. Xiao, W., Zhang, L. C., Qin, K. Z., Sun, S. & Li, J. L. Paleozoic accretionary and collisional tectonics of the Eastern Tianshan (China): Implications for the continental growth of central Asia. *Am. J. Sci.* **304**, 370–395 (2004).
27. Ma, R. S., Wang, C. Y. & Ye, S. F. The outline of plate tectonics and crustal evolution in the eastern Tianshan belt, China. *Nanjing Univ Publ House, Nanjing* **225**, (1993).
28. Hegner, E. *et al.* Mineral ages and p-t conditions of late paleozoic high-pressure eclogite and provenance of mélangé sediments from atbashi in the south tianshan orogen of kyrgyzstan. *Am. J. Sci.* **310**, 916–950 (2010).
29. Loury, C. *et al.* Tectonometamorphic evolution of the Atbashi high-P units (Kyrgyz CAOB, Tien Shan): Implications for the closure of the Turkestan Ocean and continental subduction–exhumation of the South Kazakh continental margin. *J. Metamorph. Geol.* **36**, 959–985 (2018).
30. Simonov, V. A., Sakiev, K. S., Volkova, N. I., Stupakov, S. I. & Travin, A. V. Conditions of formation of the Atbashi Ridge eclogites (South Tien Shan). *Russ. Geol. Geophys.* **49**, 803–815 (2008).
31. Loury, C., Rolland, Y., Cenko-Tok, B., Lanari, P. & Guillot, S. Late Paleozoic evolution of the South Tien Shan: Insights from P-T estimates and allanite geochronology on retrogressed eclogites (Chatkal range, Kyrgyzstan). *J. Geodyn.* **96**, 62–80 (2016).
32. Mühlberg, M. *et al.* Late Carboniferous high-pressure metamorphism of the Kassan Metamorphic Complex (Kyrgyz Tianshan) and assembly of the SW Central Asian Orogenic Belt. *Lithos* **264**, 41–55 (2016).
33. Volkova, N. I. & Budanov, V. I. Geochemical discrimination of metabasalt rocks of the Fan-Karategin transitional blueschist/greenschist belt, South Tianshan, Tajikistan: Seamount volcanism and accretionary tectonics. *Lithos* **47**, 201–216 (1999).
34. Gao, J. & Klemd, R. Formation of HP-LT rocks and their tectonic implications in the western Tianshan Orogen, NW China: Geochemical and age constraints. *Lithos* **66**, 1–22 (2003).
35. Nesbitt, H. W. & Young, G. M. Early Proterozoic climates and plate motions inferred from major elements chemistry of lutites. *Nature* **299**, 715–717 (1982).
36. Cox, R., Lowe, D. R. & Cullers, R. L. The influence of sediment recycling and basement composition on evolution of mudrock chemistry in the southwestern United States. *Geochim. Cosmochim. Acta* **59**, 2919–2940 (1995).

37. Taylor, S. R. & McLennan, S. M. The Continental Crust: its Composition and Evolution. An Examination of the Geochemical Record Preserved in Sedimentary Rocks. *Cont. Crust its Compos. Evol. An Exam. Geochemical Rec. Preserv. Sediment. Rocks.* **33**, 241–265 (1985).
38. Vermeesch, P. IsoplotR: A free and open toolbox for geochronology. *Geosci. Front.* **9**, 1479–1493 (2018).
39. Hoskin, P. W. O. & Schaltegger, U. The composition of zircon and igneous and metamorphic petrogenesis. *Rev. Mineral. Geochemistry* **53**, 27–62 (2003).
40. Sharman, G. R. & Malkowski, M. A. Needles in a haystack: Detrital zircon U-Pb ages and the maximum depositional age of modern global sediment. *Earth-Science Rev.* **203**, 103109 (2020).
41. Gehrels, G. Detrital Zircon U-Pb Geochronology Applied to Tectonics. *Annu. Rev. Earth Planet. Sci.* **42**, 127–149 (2014).
42. Song, D. *et al.* Closure of the Paleo-Asian Ocean in the Middle-Late Triassic (Ladinian-Carnian): Evidence From Provenance Analysis of Retroarc Sediments. *Geophys. Res. Lett.* **48**, 1–12 (2021).
43. Dickinson, W. R. & Gehrels, G. E. Use of U-Pb ages of detrital zircons to infer maximum depositional ages of strata: A test against a Colorado Plateau Mesozoic database. *Earth Planet. Sci. Lett.* **288**, 115–125 (2009).
44. Ge, R. *et al.* The Paleozoic northern margin of the Tarim Craton: Passive or active? *Lithos* **142–143**, 1–15 (2012).
45. Huang, H., Zhang, Z., Santosh, M., Zhang, D. & Wang, T. Petrogenesis of the early permian volcanic rocks in the Chinese South Tianshan: Implications for crustal growth in the central Asian Orogenic Belt. *Lithos* **228–229**, 23–42 (2015).
46. Ge, R. *et al.* Neoproterozoic to Paleozoic long-lived accretionary orogeny in the northern Tarim Craton. *Tectonics* **33**, 302–329 (2014).
47. Huang, H. *et al.* Early paleozoic tectonic evolution of the South Tianshan collisional belt: Evidence from geochemistry and zircon U-Pb geochronology of the tie'reke monzonite pluton, Northwest China. *J. Geol.* **121**, 401–421 (2013).
48. Zhang, C. L. & Zou, H. B. Permian A-type granites in Tarim and western part of Central Asian Orogenic Belt (CAOB): Genetically related to a common Permian mantle plume? *Lithos* **172–173**, 47–60 (2013).
49. Zhao, Z. *et al.* Early Paleozoic magmatic record from the northern margin of the Tarim Craton: Further insights on the evolution of the Central Asian Orogenic Belt. *Gondwana Res.* **28**, 328–347 (2015).
50. Wang, X. *et al.* Early Devonian tectonic conversion from contraction to extension in the Chinese Western Tianshan: A response to slab rollback. 1–21 (2020).  
doi:10.1130/B35760.1/5197886/b35760.pdf
51. Taylor, S. R. & McLennan, S. M. The geochemical the continental evolution crust. *Rev. Mineral. Geochemistry* **33**, 241–265 (1995).

52. Mao, Q. *et al.* From Ordovician nascent to early Permian mature arc in the southern Altaids: Insights from the Kalatage inlier in the Eastern Tianshan, NW China. *Geosphere* **17**, 647–683 (2021).
53. Mao, Q. *et al.* Middle Triassic lower crust-derived adakitic magmatism: Thickening of the Dananhu intra-oceanic arc and its implications for arc–arc amalgamation in the Eastern Tianshan (NW China). *Geol. J.* **56**, 3137–3154 (2021).
54. Rodríguez-Tovar, F. J. & Hernández-Molina, F. J. Ichnological analysis of contourites: Past, present and future. *Earth-Science Rev.* **182**, 28–41 (2018).
55. Rebesco, M., Hernández-Molina, F. J., Van Rooij, D. & Wåhlin, A. Contourites and associated sediments controlled by deep-water circulation processes: State-of-the-art and future considerations. *Mar. Geol.* **352**, 111–154 (2014).
56. Lin, W., Faure, M., Shi, Y., Wang, Q. & Li, Z. Palaeozoic tectonics of the south-western Chinese Tianshan: New insights from a structural study of the high-pressure/low-temperature metamorphic belt. *Int. J. Earth Sci.* **98**, 1259–1274 (2009).
57. Wang, B. *et al.* Structural and Geochronological Study of High-Pressure Metamorphic Rocks in the Kekesu Section (Northwestern China): Implications for the Late Paleozoic Tectonics of the Southern Tianshan. *J. Geol.* **118**, 59–77 (2010).
58. Jiang, T. *et al.* Paleozoic ophiolitic mélanges from the South Tianshan Orogen, NW China: Geological, geochemical and geochronological implications for the geodynamic setting. *Tectonophysics* **612–613**, 106–127 (2014).
59. Han, Y. & Zhao, G. Final amalgamation of the Tianshan and Junggar orogenic collage in the southwestern Central Asian Orogenic Belt: Constraints on the closure of the Paleo-Asian Ocean. *Earth-Science Rev.* **186**, 129–152 (2018).
60. Huang, H., Zhang, Z., Santosh, M. & Zhang, D. Geochronology, geochemistry and metallogenic implications of the Boziguo'er rare metal-bearing peralkaline granitic intrusion in South Tianshan, NW China. *Ore Geol. Rev.* **61**, 157–174 (2014).
61. Konopelko, D., Biske, G., Seltmann, R., Eklund, O. & Belyatsky, B. Hercynian post-collisional A-type granites of the Kokshaal Range, Southern Tien Shan, Kyrgyzstan. *Lithos* **97**, 140–160 (2007).
62. Seltmann, R., Konopelko, D., Biske, G., Divaev, F. & Sergeev, S. Hercynian post-collisional magmatism in the context of Paleozoic magmatic evolution of the Tien Shan orogenic belt. *J. Asian Earth Sci.* **42**, 821–838 (2011).
63. Liu, X. *et al.* The youngest Permian Ocean in Central Asian Orogenic Belt: Evidence from Geochronology and Geochemistry of Bingdaban Ophiolitic Mélange in Central Tianshan, northwestern China. *Geol. J.* **55**, 2062–2079 (2020).
64. Sang, M., Xiao, W., Feng, Q. & Windley, B. F. Radiolarian age and geochemistry of cherts from the Atbashi accretionary complex, Kyrgyz South Tianshan. *Geol. J.* 1–10 (2020). doi:10.1002/gj.3952
65. Li, R. *et al.* The discovery of Carboniferous-Permian radiolarians from the upatarkan group in the western South Tianshan. *Chinese J. Geol.* **40**, 220–226 (2005).

66. Agard, P., Yamato, P., Jolivet, L. & Burov, E. Exhumation of oceanic blueschists and eclogites in subduction zones: Timing and mechanisms. *Earth-Science Rev.* **92**, 53–79 (2009).
67. Rodríguez-González, J., Negrodo, A. M. & Billen, M. I. The role of the overriding plate thermal state on slab dip variability and on the occurrence of flat subduction. *Geochemistry, Geophys. Geosystems* **13**, 1–21 (2012).
68. Ao, S. *et al.* The youngest matrix of 234 Ma of the Kangur accretionary mélange containing blocks of N-MORB basalts: constraints on the northward subduction of the Paleo-Asian Kangur Ocean in the Eastern Tianshan of the Southern Altai. *Int. J. Earth Sci.* **110**, 791–808 (2021).
69. Zhang, J., Wei, C. & Chu, H. Blueschist metamorphism and its tectonic implication of Late Paleozoic–Early Mesozoic metabasites in the mélange zones, central Inner Mongolia, China. *J. Asian Earth Sci.* **97**, 352–364 (2015).
70. Li, S. *et al.* Linking magmatism with collision in an accretionary orogen. *Sci. Rep.* **6**, 1–12 (2016).
71. Li, S. *et al.* Early-Middle Triassic high Sr/Y granitoids in the southern Central Asian Orogenic Belt: Implications for ocean closure in accretionary orogens. *J. Geophys. Res. Solid Earth* **122**, 2291–2309 (2017).
72. Ramos, V. A. & Folguera, A. Andean flat-slab subduction through time. *Geol. Soc. Spec. Publ.* **327**, 31–54 (2009).
73. Axen, G. J., van Wijk, J. W. & Currie, C. A. Basal continental mantle lithosphere displaced by flat-slab subduction. *Nat. Geosci.* **11**, 961–964 (2018).
74. Manea, V. C. *et al.* A review of the geodynamic evolution of flat slab subduction in Mexico, Peru, and Chile. *Tectonophysics* **695**, 27–52 (2017).
75. Rosenbaum, G. *et al.* Subduction of the Nazca Ridge and the Inca Plateau: Insights into the formation of ore deposits in Peru. *Earth Planet. Sci. Lett.* **239**, 18–32 (2005).
76. Li, Z. X. & Li, X. H. Formation of the 1300-km-wide intracontinental orogen and postorogenic magmatic province in Mesozoic South China: A flat-slab subduction model. *Geology* **35**, 179–182 (2007).
77. Dickinson, W. R. Potash-Depth (K-h) relations in continental margin and intra-oceanic magmatic arcs. *Geology* **3**, 53–56 (1975).
78. Wang, B. *et al.* Accretionary tectonics of back-arc oceanic basins in the South Tianshan: Insights from structural, geochronological, and geochemical studies of the Wuwamen ophiolite mélange. *Bull. Geol. Soc. Am.* **130**, 284–306 (2018).
79. Wan, B. *et al.* Long-lived seamount subduction in ancient orogens: Evidence from the Paleozoic South Tianshan. **XX**, 1–5 (2021).
80. Manea, V. C., Marta, P. G. & Manea, M. Chilean flat slab subduction controlled by overriding plate thickness and trench rollback. *Geology* **40**, 35–38 (2012).
81. Hu, J. & Liu, L. Abnormal seismological and magmatic processes controlled by the tearing South American flat slabs. *Earth Planet. Sci. Lett.* **450**, 40–51 (2016).

82. Bayon, G. *et al.* Hf and Nd isotopes in marine sediments: Constraints on global silicate weathering. *Earth Planet. Sci. Lett.* **277**, 318–326 (2009).
83. Van Hunen, J., Van Den Berg, A. P. & Vlaar, N. J. On the role of subducting oceanic plateaus in the development of shallow flat subduction. *Tectonophysics* **352**, 317–333 (2002).
84. Van Orman, J. A., Grove, T. L., Shimizu, N. & Layne, G. D. Rare earth element diffusion in a natural pyrope single crystal at 2.8 GPa. *Contrib. to Mineral. Petrol.* **142**, 416–424 (2002).
85. Gerya, T. V., Fossati, D., Cantieni, C. & Seward, D. Dynamic effects of aseismic ridge subduction: numerical modelling. *Eur. J. Mineral.* **21**, 649–661 (2009).
86. Wang, X. *et al.* Geochemistry and geochronology of the Precambrian high-grade metamorphic complex in the Southern Central Tianshan ophiolitic mélange, NW China. *Precambrian Res.* **254**, 129–148 (2014).
87. Huang, H. *et al.* Rejuvenation of ancient micro-continents during accretionary orogenesis: Insights from the Yili Block and adjacent regions of the SW Central Asian Orogenic Belt. *Earth-Science Rev.* **208**, 103255 (2020).
88. Liu, S. & Currie, C. A. Farallon plate dynamics prior to the Laramide orogeny: Numerical models of flat subduction. *Tectonophysics* **666**, 33–47 (2016).
89. O’Driscoll, L. J., Richards, M. A. & Humphreys, E. D. Nazca-South America interactions and the late Eocene-late Oligocene flat-slab episode in the central Andes. *Tectonics* **31**, 1–16 (2012).
90. Manea, V. C., Manea, M. & Ferrari, L. A geodynamical perspective on the subduction of Cocos and Rivera plates beneath Mexico and Central America. *Tectonophysics* **609**, 56–81 (2013).
91. Charvet, J., Shu, L. & Laurent-Charvet, S. Paleozoic structural and geodynamic evolution of eastern Tianshan (NW China): Welding of the Tarim and Junggar plates. *Episodes* **30**, 162–186 (2007).
92. Laurent-Charvet, S., Charvet, J., Monié, P. & Shu, L. Late Paleozoic strike-slip shear zones in eastern central Asia (NW China): New structural and geochronological data. *Tectonics* **22**, (2003).
93. Zong, K. *et al.* The assembly of Rodinia: The correlation of early Neoproterozoic (ca. 900 Ma) high-grade metamorphism and continental arc formation in the southern Beishan Orogen, southern Central Asian Orogenic Belt (CAOB). *Precambrian Res.* **290**, 32–48 (2017).
94. Hu, Z. *et al.* ‘Wave’ signal-smoothing and mercury-removing device for laser ablation quadrupole and multiple collector ICPMS analysis: Application to lead isotope analysis. *Anal. Chem.* **87**, 1152–1157 (2015).
95. Liu, Y. *et al.* Continental and oceanic crust recycling-induced melt-peridotite interactions in the Trans-North China Orogen: U-Pb dating, Hf isotopes and trace elements in zircons from mantle xenoliths. *J. Petrol.* **51**, 537–571 (2009).
96. Ludwig, K. R. A Geochronological Toolkit for Microsoft Excel. *Berkeley Geochronol. Center, Spec. Publ.* **4**, 71 (2003).
97. Tan, Z., Agard, P., Gao, J., Hong, T. & Wan, B. Concordant pulse in Mn, Y and HREEs concentrations during UHP eclogitic garnet growth: Transient rock dynamics along a cold subduction plate interface.

- Earth Planet. Sci. Lett.* **530**, 115908 (2020).
98. Bayet, L. *et al.* Tectonic evolution of the Tianshan Akeyazi metamorphic complex (NW China). *Lithos* **354–355**, 105273 (2020).
99. Whitney, D. L. & Evans, B. W. Abbreviations for names of rock-forming minerals. *Am. Mineral.* **95**, 185–187 (2010).
100. Dickinson, W. *et al.* Provenance of North American Phanerozoic sandstones in relation to tectonic setting. *Geol. Soc. Am. Bull.* **94**, 222–235 (1983).
101. Floyd, P. A. & Leveridge, B. E. Tectonic environment of the Devonian Gramscatho basin, south Cornwall: framework mode and geochemical evidence from turbiditic sandstones (England). *J. Geol. Soc.* **144**, 531–542 (1987).
102. Roberta L Rudnick, D. M. F. Nature and Composition of the Continental Crust; A Lower Crustal Perspective. *Rev. Geophys.* **33**, 1–43 (2007).
103. Bhatia, M. R. & Crook, K. A. W. Trace element characteristics of graywackes and tectonic setting discrimination of sedimentary basins. *Contrib. to Mineral. Petrol.* **92**, 181–193 (1986).
104. Sun, S. S. & McDonough, W. F. Chemical and isotopic systematics of oceanic basalts: Implications for mantle composition and processes. *Geol. Soc. Spec. Publ.* **42**, 313–345 (1989).
105. Chiaradia, M. Crustal thickness control on Sr/Y signatures of recent arc magmas: An Earth scale perspective. *Sci. Rep.* **5**, 8115 (2015).
106. Sang, M., Xiao, W. & Windley, B. F. Unravelling a Devonian–Triassic seamount chain in the South Tianshan high-pressure/ultrahigh-pressure accretionary complex in the Atbashi area (Kyrgyzstan). *Geol. J.* 2300–2317 (2020). doi:10.1002/gj.3776
107. Zhang, D. *et al.* Perovskite and baddeleyite from kimberlitic intrusions in the Tarim large igneous province signal the onset of an end-Carboniferous mantle plume. *Earth Planet. Sci. Lett.* **361**, 238–248 (2013).
108. Wei, X., Xu, Y. G., Feng, Y. X. & Zhao, J. X. Plume-lithosphere interaction in the generation of the Tarim large igneous province, NW China: Geochronological and geochemical constraints. *Am. J. Sci.* **314**, 314–356 (2014).
109. Li, X. P., Zhang, L. F., Wilde, S. A., Song, B. & Liu, X. M. Zircons from rodingite in the Western Tianshan serpentinite complex: Mineral chemistry and U-Pb ages define nature and timing of rodingitization. *Lithos* **118**, 17–34 (2010).

## Figures

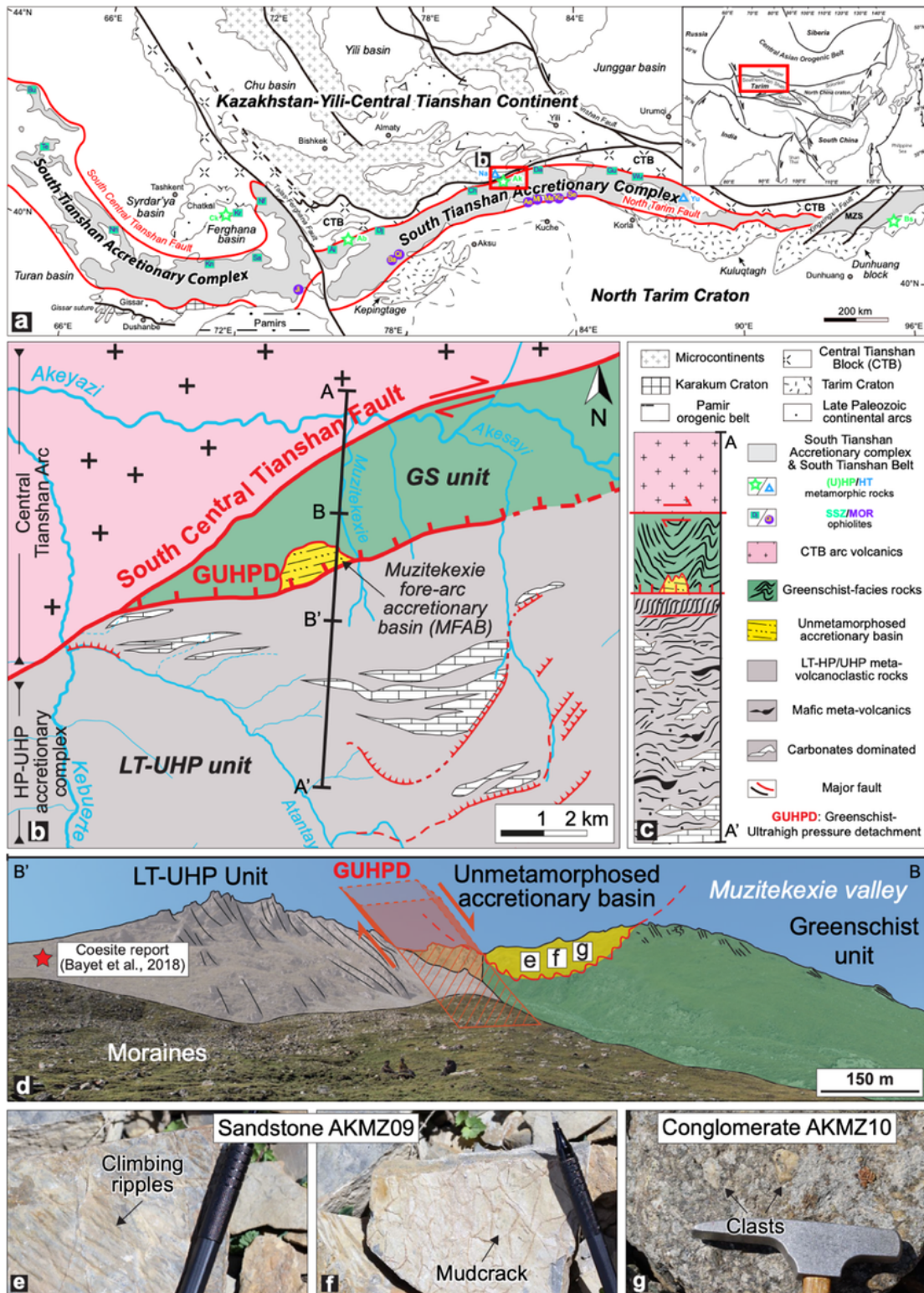
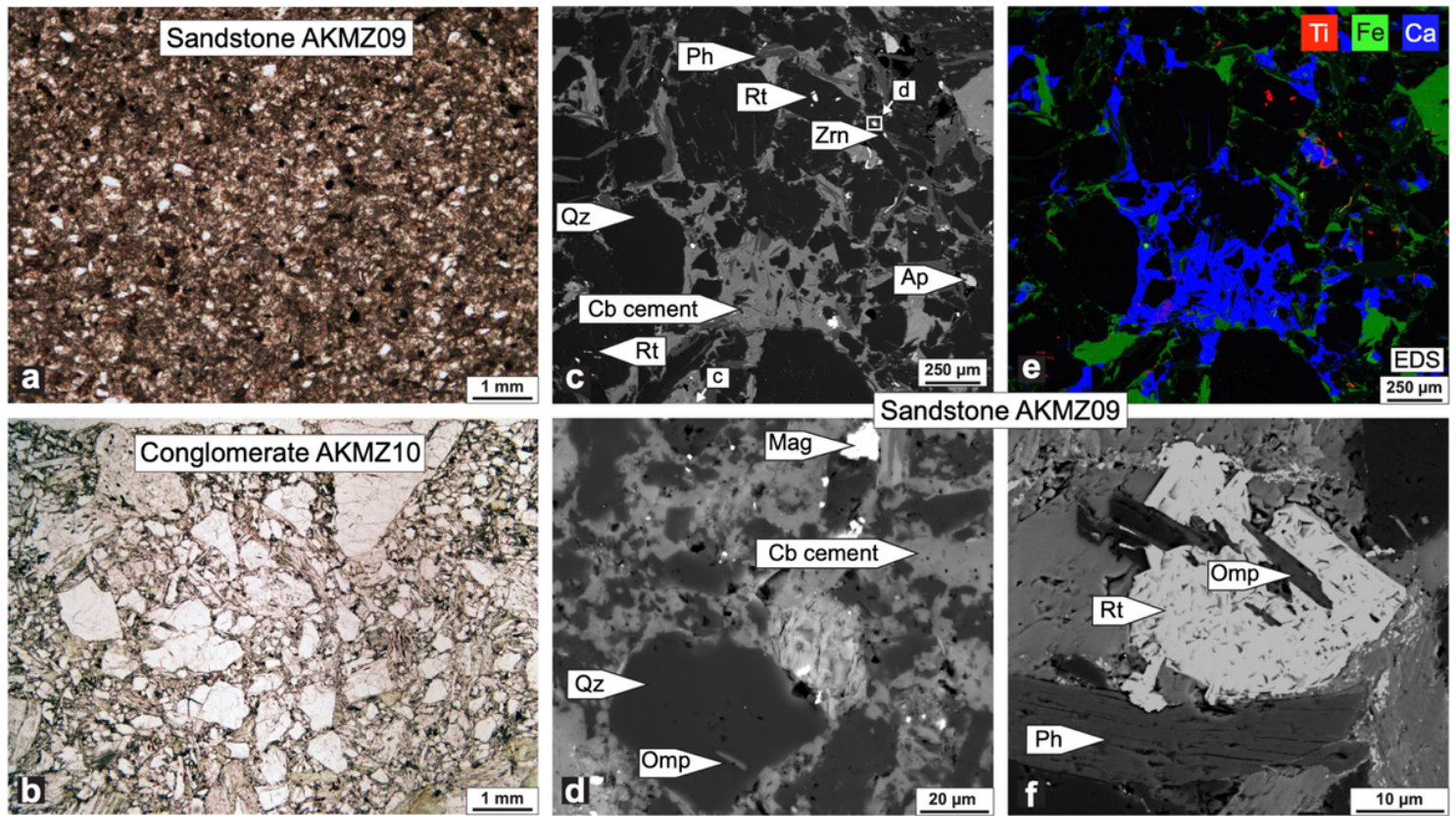


**Figure 1**

**Tectonic framework and outlook of studied area.** a) Map of the southern Altai, modified after ref<sup>14</sup>. b) Regional geological map of the AMC in Chinese STO, modified after refs<sup>97,98</sup>. c) Synthetic and schematic lithological profile, along the cross-section from north (top, A) to south (bottom, A'). d) Field view of the Muzetekxie valley, modified after<sup>98</sup>; the dotted part of the line represents a more diffuse nature of this contact, and the studied unmetamorphosed basin is unconformably overlying the greenschist-unit. e)

Climbing ripples observed in sandstone outcrops. f) Mud-crack preserved in sandstone crops. g) Several cent-meters scale clasts in conglomerate outcrop.



**Bulk-rock composition**

**Key minerals composition**

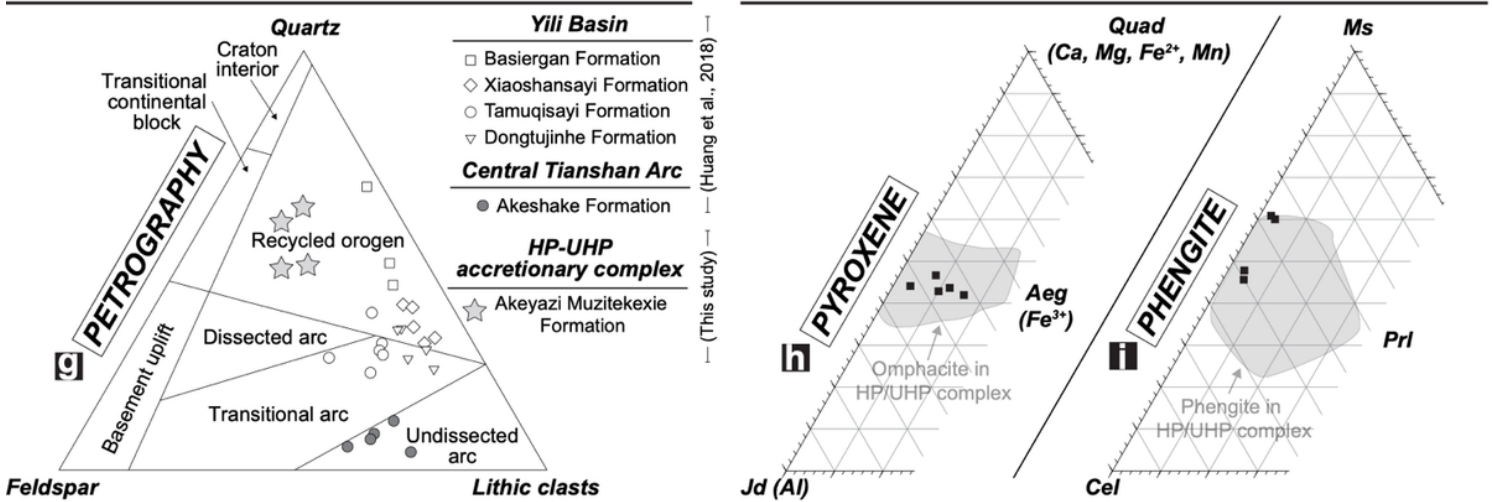
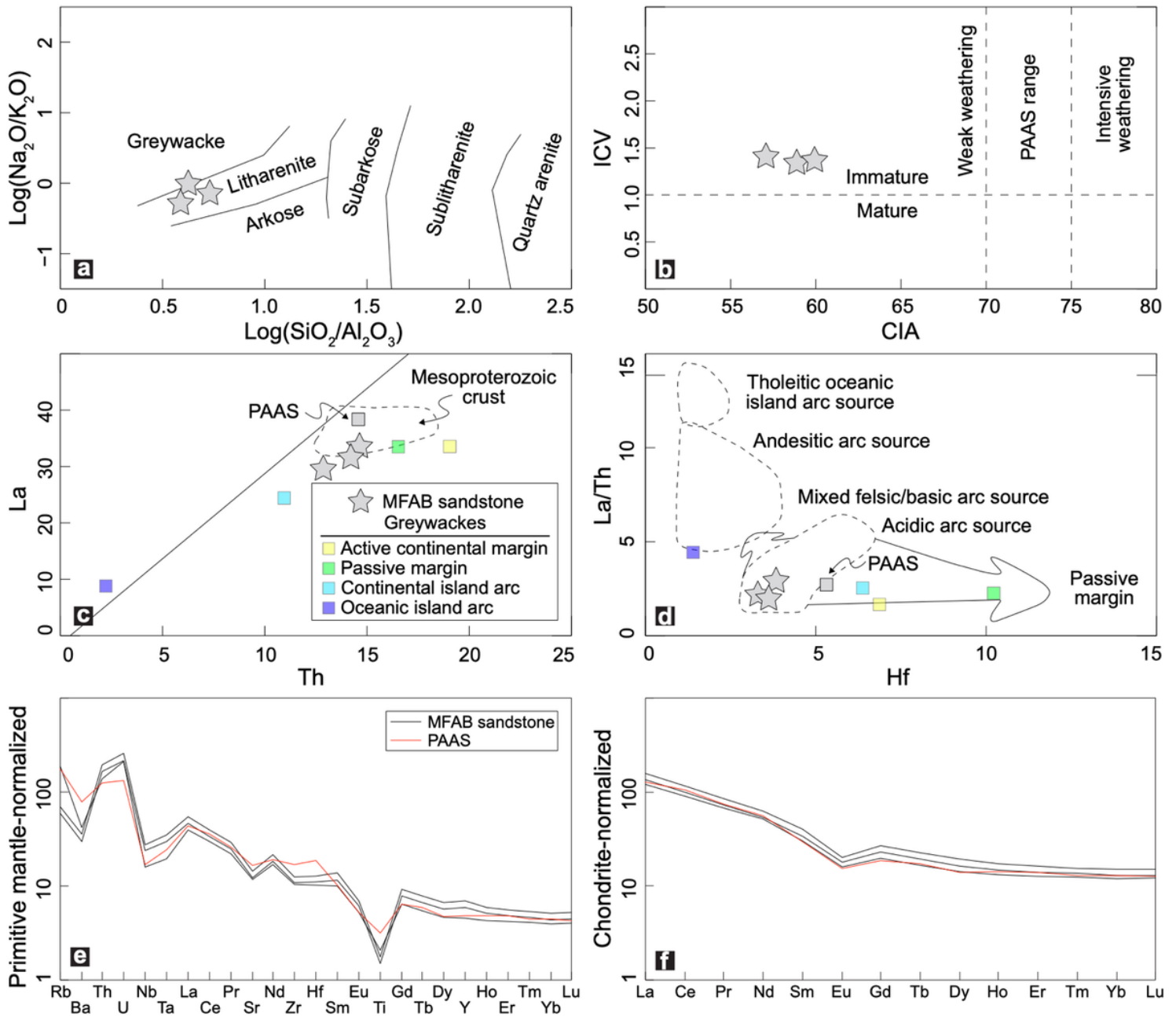


Figure 2

**Petrographic features of the MFAB sandstone.** a) Triassic sandstones and b) conglomerates in the MFAB. c, d, f) BSE images and e) SEM-EDS mapping show the preservation of high-pressure mineral relics (i.e., Rt, Ph and Omp) in detritus; mineral abbreviation is following ref<sup>99</sup>. g) Sandstone petrographic data for studied samples including Q-F-L<sup>100</sup> (quartz, feldspar and lithic clasts). h, i) Mineral composition of phengite and omphacite relics found in studied sandstones.



**Figure 3**

**Geochemical classification and discrimination of the MFAB sandstones.** a)  $\log(\text{Na}_2\text{O}/\text{K}_2\text{O})$  vs  $\log(\text{SiO}_2/\text{Al}_2\text{O}_3)$  and b) ICV vs CIA for studied sandstones; the index of chemical alteration, CIA =  $[\text{Al}_2\text{O}_3/(\text{Al}_2\text{O}_3 + \text{CaO}^* + \text{Na}_2\text{O} + \text{K}_2\text{O})] \times 100$ , where CaO\* is the content of CaO in silicate minerals only, is given after ref<sup>35</sup> and the Index of Compositional Variability, ICV =  $(\text{CaO} + \text{K}_2\text{O} + \text{Na}_2\text{O} + \text{Fe}_2\text{O}_3 + \text{MgO} + \text{MnO} + \text{TiO}_2)/\text{Al}_2\text{O}_3$  is given after ref<sup>36</sup>. c) La vs Th; d) La/Th vs Hf after ref<sup>101</sup>; sources: Mesoproterozoic crust<sup>102</sup>, PAAS<sup>37</sup>, ref for average greywacke compositions<sup>103</sup>. e-f) spider and REEs pattern diagrams of studied sandstones; values of primitive mantle<sup>104</sup>, chondrite<sup>104</sup> and PAAS<sup>37</sup> are used for normalization and comparison.

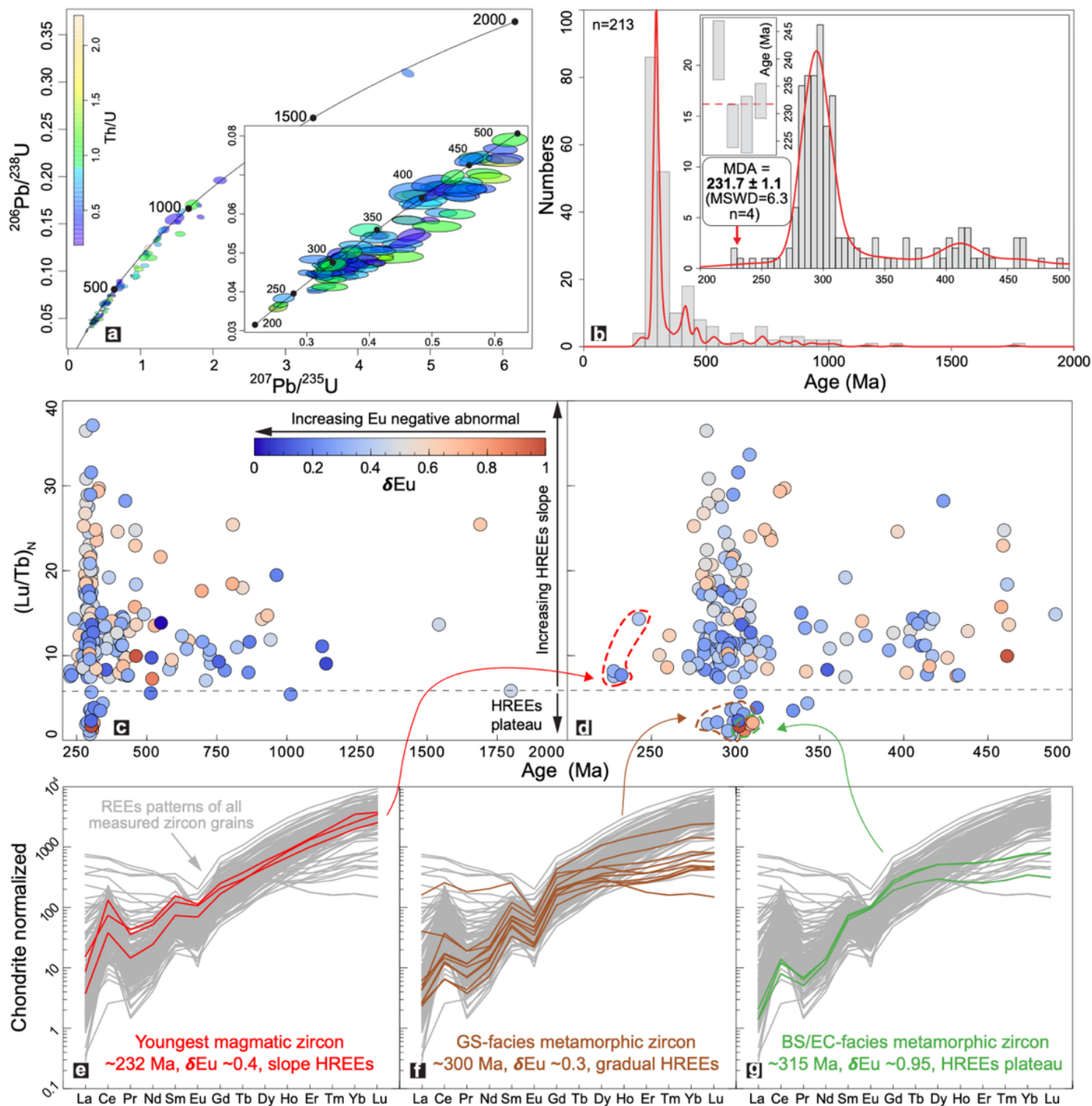


**Figure 4**

**Detrital zircon U-Pb isotopic and rare earth elements (REEs) results.** a-b) Detrital zircon U-Pb concordia and KDE plots of the MFAB sandstones. c-g) Diagrams of ages versus detrital zircon rare earth elements characters (denoted by  $\delta\text{Eu}$ ,  $(\text{Lu}/\text{Tb})_N$  and REEs pattern) to deduce the multiple detritus provenance.

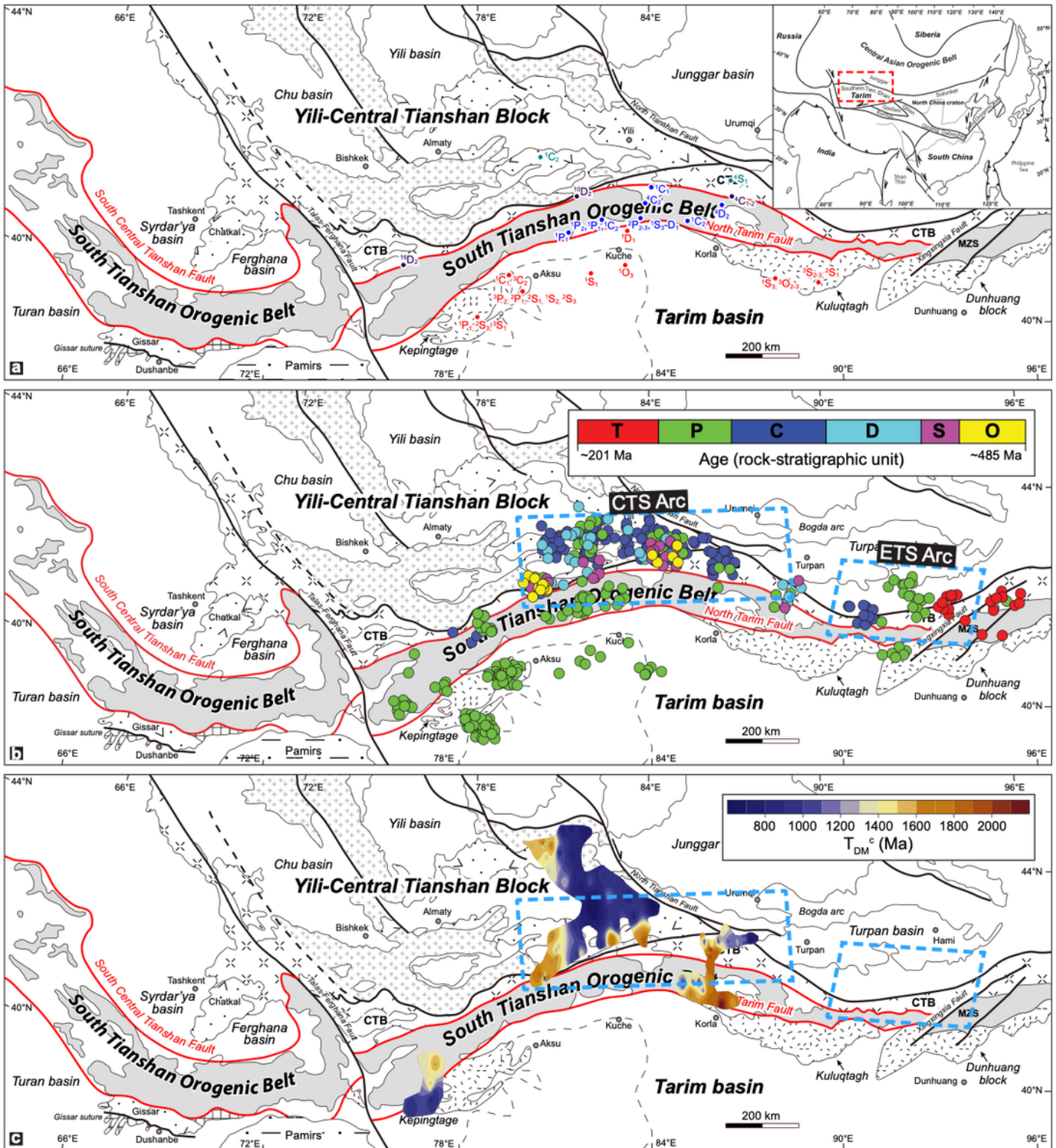


Figure 5

Geological maps with the highlighted localities of compiled multi-disciplinary data. a) collected detrital zircon U-Pb ages of regional sediments (corresponding to data in Table S7), b) compiled zircon U-Pb ages of regional intermediate rocks (corresponding to data in Table S6). c) Hf isotope contour map after ref<sup>87</sup>,

based on Paleozoic granitoid rocks and felsic volcanic rocks among the STOB, showing the spatial variation of ancient crustal basement (fragmented craton or micro-continent) with relative old Hf model ages.

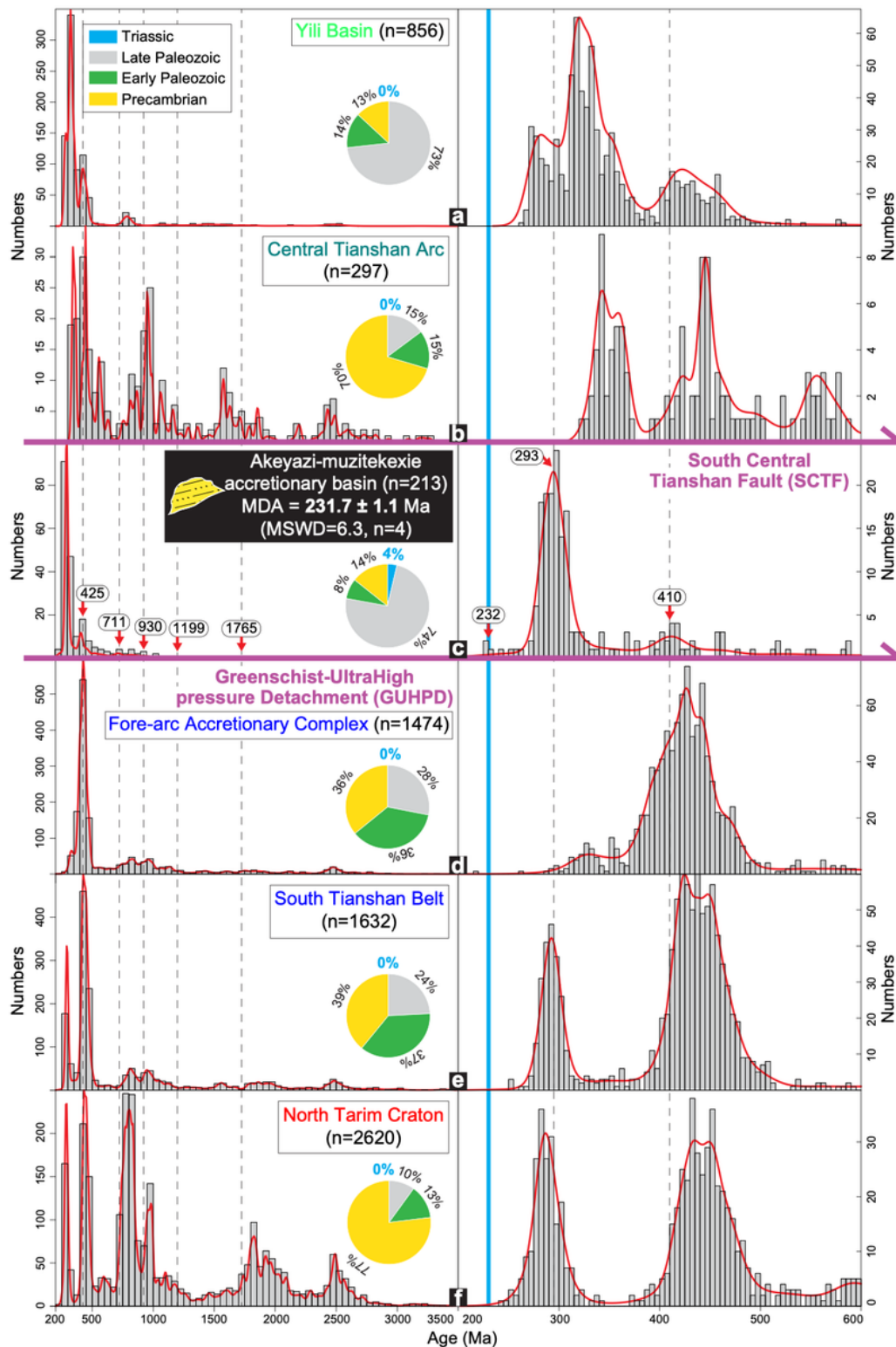


Figure 6

KDE plots of detrital zircon U-Pb ages of sediments in adjacent key tectonic units. a) Yili Basin, b) Central Tianshan Arc, c) Triassic MAFB (this study), d) Fore-arc accretionary Complex, e) South Tianshan Belt and f) North Tarim Craton. The proportion of Triassic, late Paleozoic, early Paleozoic and Precambrian detrital zircons, as well as the maximum depositional ages (MDA, blue solid-line) of Triassic MAFB, are highlighted for comparison. Relevant data is listed in Table S2 and S7.

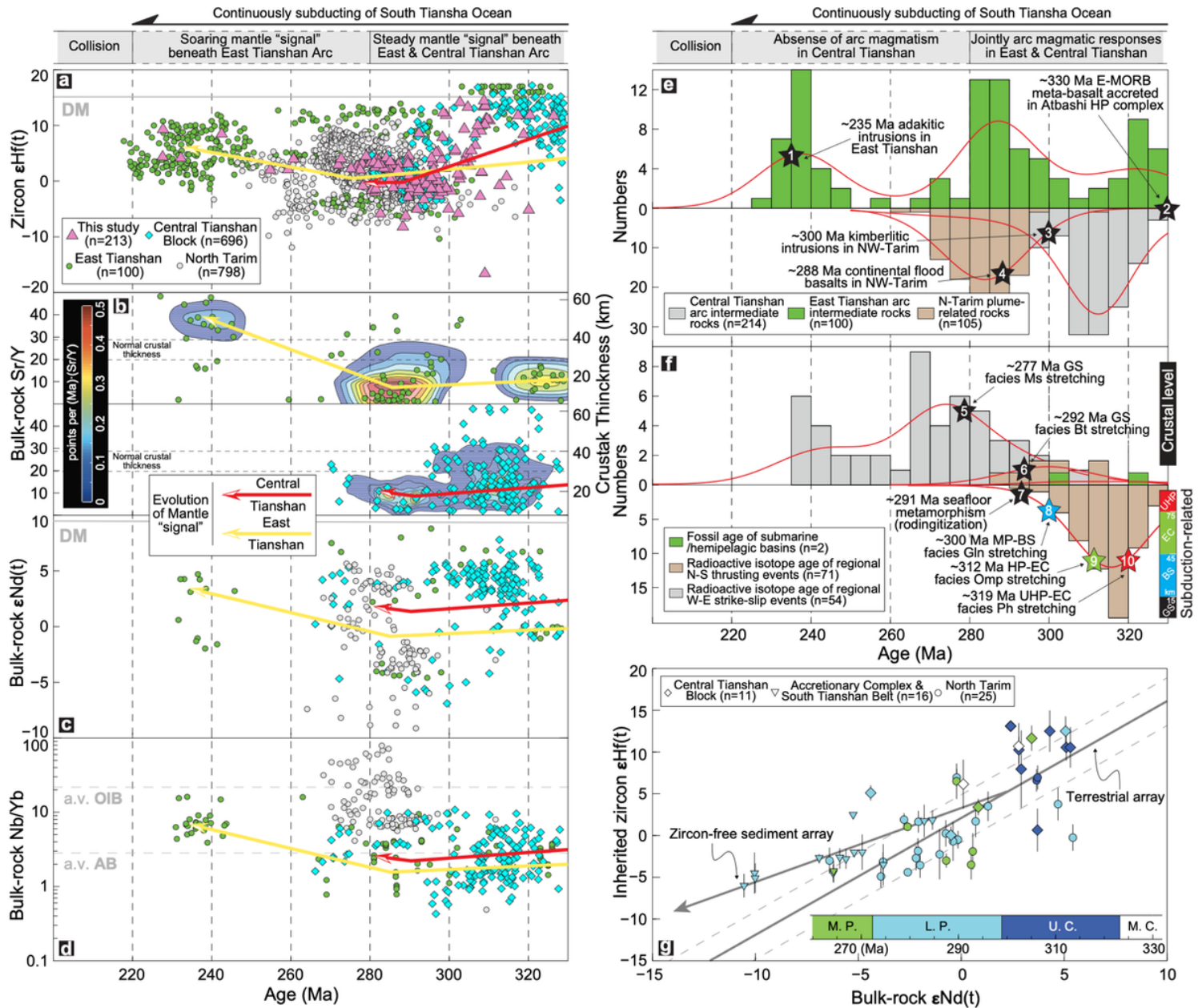


Figure 7

Plots of compiled multi-disciplinary evidence. It shows the spatial-temporal evolution of a) inherited & detrital zircon  $\epsilon Hf(t)$ , b) bulk-rock Sr/Y, c)  $\epsilon Nd(t)$  and d) Nb/Yb of arc intermediate rocks among the MAFB, CTS, ETS region and NTC; crustal thickness is derived from the method of ref<sup>105</sup>; yellow and red arrows indicate the evolution of mantle "signal" respectively beneath ETS and CTS Arc regions. e) KDE

plot of ages of regional arc intermediate rocks; ages marked by numbers 1-4 with black star are respectively cited from refs<sup>53,106-108</sup>. f) KDE plot of ages of regional metamorphism, depositing and main strike-slip faulting & thrusting events; ages marked by numbers 5-10 with black, colored stars are respectively cited from refs<sup>22,109</sup>. g) Bulk rock  $\epsilon\text{Nd}(t)$ -zircon  $\epsilon\text{Hf}(t)$  isotope diagram for ~260-330 Ma arc or plume-related intermediate rocks from regional tectonic units. Relevant data is presented in Tables S2-S4. Compiled regional data is listed in Tables S6-S7.

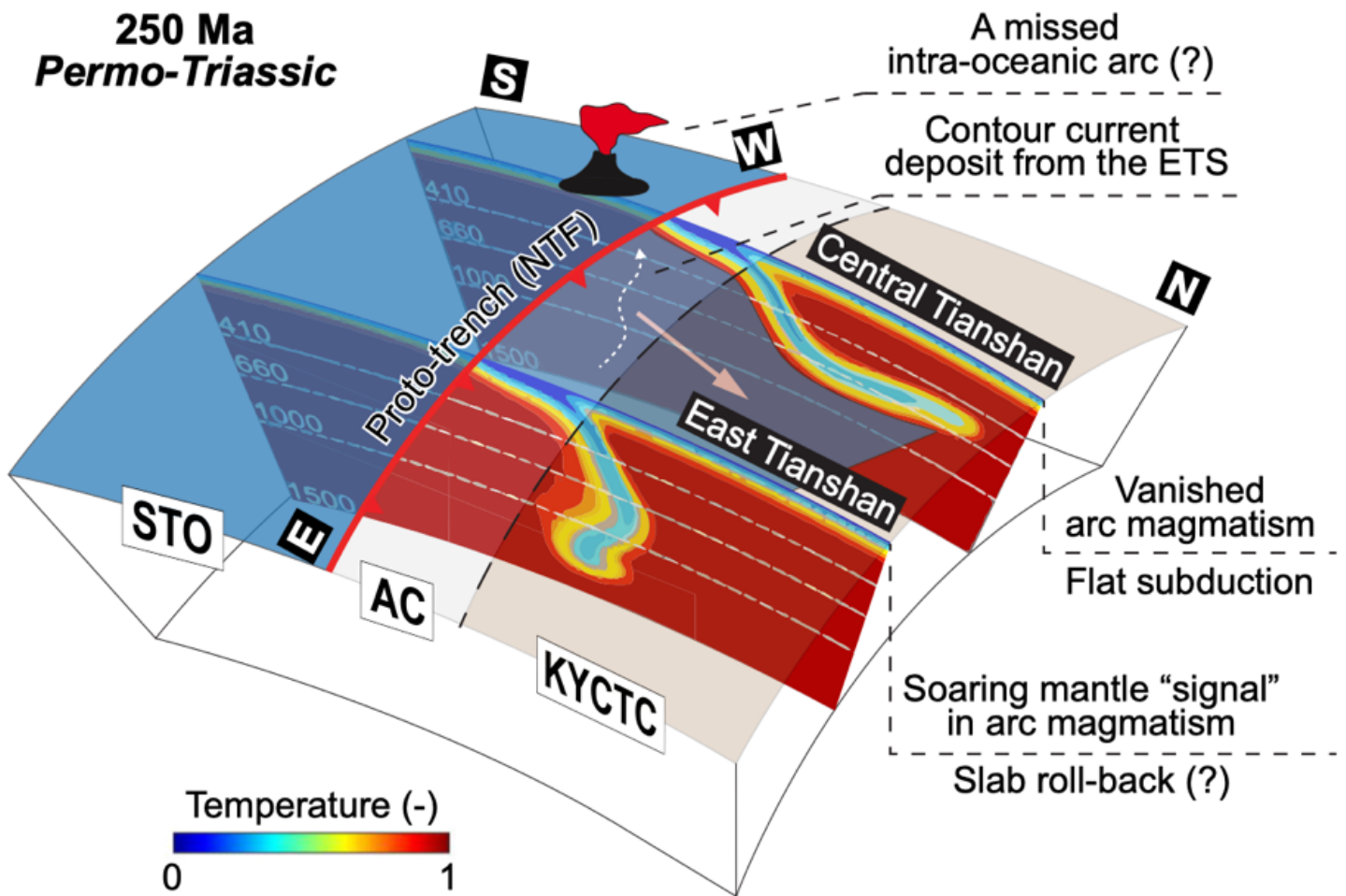


Figure 8

An updated geodynamic model for the Permo-Triassic (~250 Ma) evolution of the South Tianshan Ocean (STO). The trench-parallel slab geometry “anisotropy” (i.e., temporary flat subduction beneath the CTS region in the KYCTC), during which witnesses its fate from the Triassic to Permian, is highlighted. AC: accretionary complex; KYCTC: Kazakhstan-Yili-Central Tianshan Continent. The schematic diagrams of various slab geometry are cited from results of numerical modeling by ref<sup>80</sup>.

# Supplementary Files

This is a list of supplementary files associated with this preprint. Click to download.

- [SupplementaryTableX1.pdf](#)
- [SupplementaryTableX2.pdf](#)
- [SupplementaryTableX3.pdf](#)
- [SupplementaryTableX4.pdf](#)
- [SupplementaryTableX5.pdf](#)
- [SupplementaryTableX6.pdf](#)
- [SupplementaryTableX7.pdf](#)
- [SupplementaryTableX8.pdf](#)
- [SupplementaryTableX9.pdf](#)
- [SupportingInformation.pdf](#)